Nanoscale

Pt Alloy Nanoparticles Decorated on Large-Size Nitrogen-Doped Graphene Tubes for Highly Stable Oxygen-Reduction Catalysts

SCHOLARONE™
Manuscripts

Nanoscale

ARTICLE

Pt Alloy Nanoparticles Decorated on Large-Size Nitrogen-Doped Graphene Tubes for Highly Stable Oxygen-Reduction Catalysts

Mengjie Chen,[a,1] Sooyeon Hwang, [b,1] Jiazhan Li,[a] Stavros Karakalos,[c] Kate Chen,[a] Yanghua He,[a] Shreya Mukherjee,[a] Dong Su,[b,*] and Gang Wu[a,*]

Pt alloy nanoparticles supported on Vulcan XC-72 (Pt/C) are the most effective catalysts for kinetically sluggish oxygen reduction reaction (ORR) in proton exchange membrane fuel cells. However, significant performance degradation has been observed with the Pt/C catalysts due to agglomeration and Ostwald ripening of Pt nanoparticles largely resulting from the corrosion of carbon supports. Here, we developed a catalyst of Pt alloy nanoparticles deposited on nitrogen/metal co-doped large-size graphene tubes (NGTs). The formation of PtM (M: Co and Ni) alloy during the subsequent annealing process contributes to the improvement of the catalytic activity. More importantly, the nanocomposite of PtM alloy and NGTs exhibits exceptionally enhanced stability. During the accelerated stress tests (AST), after 20,000 potential cycles (0.6-1.0 V vs. RHE), the retained electrochemical surface area (ECSA) of the PtM/NGT catalyst is more than 2 times larger than that of Pt/C catalyst. As for the AST tests for carbon corrosion, after 30,000 potential cycles (1.0-1.5 V vs. RHE) at room temperature, the NGT morphologies are well maintained and no ECSA loss of this PtM catalyst is observed, indicating excellent corrosion-resistance. Even at harsher 60°C, the PtM/NGT catalyst exhibits only insignificant loss (6 mV) of $E_{1/2}$ while the Pt/C catalyst shows significant degradation (47 mV loss in $E_{1/2}$). The improved stability of PtM/NGT catalyst is attributed to the highly graphitized NGTs and possible synergistic effects between the NGT carbon support and the PtM alloy nanoparticles.

Introduction

In recent years, polymer electrolyte membrane fuel cells (PEMFCs) have been widely developed as power sources of the future for clean energy application, such as electric vehicles, consumer electronics, and stationary power.[1, 2] The oxygen reduction reaction (ORR) is considered as a kinetic barrier for fuel cell operation. At present, Pt alloy supported on Vulcan XC-72 remains the most effective catalyst to catalyze the sluggish ORR in both acidic and alkaline solution for such clean energy technologies.[3, 4] However, the scarcity and prohibitively high price of Pt have been major hurdles which limit the large-scale application of this catalyst. Furthermore, Pt agglomeration can be induced by degradation of the electrochemical active surface area (ECSA) and oxidation of carbon support, which would deteriorate the performance of cathode.[5-8]

The formation of Pt-based alloy is one effective method to achieve enhanced activity and stability of Pt catalysts due to the strain and electronic effects.[9] Compared to pure Pt cathode catalysts in PEMFCs, Pt-based alloys have exhibited better electrocatalytic activity and stability for the oxygen reduction reaction.[10-12] By alloying Pt with 3d transition metals (Co, Ni, Cr, Fe, *etc.*), the formation of PtO_2 will be suppressed and Pt-Pt interatomic distance will be decreased, resulting in less Pt dissolution and more favorable O_2 adsorption.[13, 14] Thus, superior durability and high mass activity for oxygen reduction reaction (ORR) could be obtained. Among these Pt-M alloy catalysts, the Pt-Co and Pt-Ni alloy catalysts have attracted much more attention because of their superior performance in acid media. It has been found that Pt-Co and Pt-Ni catalysts perform more favorable ORR kinetics than other Pt-M alloy catalysts.[15-17] Mass activity (MA), specific activity (SA), and durability of Pt-Co and Pt-Ni alloy catalysts are also significantly improved than the commercial Pt/C cathode catalyst.[16-18]

Another effective strategy for enhancing catalytic properties focuses on the selection of a support. Many advanced carbon materials, such as carbon nanotubes[19-21], graphene[22, 23], and carbon nanofibers[24], have been widely used as support to improve the distribution and utilization of Pt nanoparticles due to their high electric conductivity, unique structures, and high surface areas. Although these carbon materials can effectively disperse Pt nanoparticles and promote Pt utilization, they have poor corrosion resistance and little catalytic activity towards ORR. As a result, the activity and stability of these catalysts are still hard to meet the requirements for large-scale applications. Therefore, it is crucial to find a stable and active carbon material. Interestingly, the microstructure and electronic

[a.] Department of Chemical and Biological Engineering, University at Buffalo, The State University of New York, Buffalo, New York 14260, United States
Email: gangwu@buffalo.edu
[b.] Center for Functional Nanomaterials, Brookhaven National Laboratory, Upton, NY 11973, United States
Email: dsu@bnl.gov
[c.] Department of Chemical Engineering, University of South Carolina, Columbia, SC 29208, United States
1 These two authors contributed equally.
Electronic Supplementary Information (ESI) available: See DOI: 10.1039/x0xx00000x

transport of carbon materials can be modified by introducing heteroatoms.[25] Previous works have exhibited significantly enhanced ORR activity of carbon materials by doping heteroatoms (*e.g.* N, P, S) and transition metals (*e.g.* Fe, Co) in aqueous electrolyte, while maintaining their intrinsic structure and robust morphology.[25-29] In these cases, carbon materials not only play a role as ORR catalyst, but also as the support. Pt nanoparticles can successfully deposit on nitrogen-doped carbon materials and these catalysts showed enhanced activity and stability than Pt supported on pure carbon materials, indicating that the nitrogen-doping is important to enhance the performance of Pt cathode catalysts.[30-32]

Herein, we provide a new design strategy of highly active and stable ORR catalysts by innovatively integrating nitrogen/metal co-doped graphene tubes (NGTs) and Pt nanoparticles in a unique hybrid configuration. The NGTs, which are synthesized via a carbonization of dicyandiamide with transition metals (Co and Ni), have a highly graphitized structure with transition metal/nitrogen co-doping. Thus, the novel NGTs materials not only show excellent corrosion resistance but also generate a lot of additional ORR-active sites, thereby remarkably enhancing the ORR activity and durability of the Pt catalysts. Moreover, Pt could be integrated with the doped transition metals in the carbon matrix to form Pt-M (M is Co/Ni) alloy structure during the thermal conversion, resulting in lower O_2 adsorption energy and less Pt oxidation. Additionally, the possible synergistic effect was also observed between Pt and NGTs, which further boost the performance of such a Pt-based cathode catalyst. Consequently, the ORR kinetics can be highly favored and stability of catalysts can be significantly improved.

Results and discussion

Characterization of nitrogen-doped graphene tubes

Herein, we synthesized three different graphene tube supports derived from different metal precursors, i.e. CoNi, Co, and Ni, which were labeled as NGT(CoNi), NGT(Co), and NGT(Ni), respectively. It is well known that the Fenton reaction is initiated by active redox pairs of Fe(II)/Fe(III). Both Fe(II) and Fe(III) are very active and common species. As for Co and Ni, only Co(II) and Ni(II) are comparably stable species. It is hard for them to be oxidized by H_2O_2 and initiate the Fenton reaction for radical generation.[33,34] Therefore, Fe-derived graphene tubes were not studied in this research. Afterwards, Pt nanoparticles were deposited on graphene tubes via a chemical reduction method followed by a heating treatment (**Figure 1**) and these Pt-based catalysts were screened by accelerated stressed tests (ASTs) with different potential ranges. More details of synthesis and electrochemical measurement can be found from the experimental section in the supporting information.

To reveal the carbon morphology of graphene tubes, scanning electron microscopy (SEM) was performed. As depicted in **Figure 2a**, **2b** and **2c**, isolated and well-defined tubular morphology was observed for samples derived from different transition metals. Typically, NGT(CoNi) yielded the largest width ranging from 150 nm to 350 nm, followed by NGT(Co) and NGT(Ni). It should be noted that it is more difficult

to deposit Pt onto a tube with smaller size such as traditional carbon nanotubes (CNTs). The NGTs with large size can provide much more uniform particle distribution than traditional carbon nanotubes.

Raman characterization was performed to further study carbon structures in various NGTs. As shown in **Figure 2d**, following the convention of Cuesta et al.[35] and Bonhomme et al.[36] for polycrystalline graphitic materials, four bands approximately at 1230, 1350, 1488, and 1580 cm^{-1} referred to I, D, D´´, and G were incorporated into fitting for the studied NGT supports derived from various metal precursors. For all the samples, the G and D bands are the most intense first order spectral modes. The G band corresponds to the high-frequency E_{2g} phonon resulting from sp^2 hybridized C-C bonds in a two-dimensional hexagonal lattice. The D band results from the defects or disordered carbon atoms of six-side hexagonal rings.[37-39] In general, the ratio of the relative intensity of D to G band (I_D/I_G) can be an indicator of graphitization degree of carbon structure. As a result, the NGT(Co) showed the highest graphitization degree (I_D/I_G = 0.71), while NGT (Ni) presents the lowest degree among these three supports. In addition, G' band at 2600 cm^{-1}, an overtone mode of D band, also present in all these samples. Its appearance does not require the presence of defects/disorder in graphite structure. However, its intensity was found to be highly sensitive to nitrogen doping level and type as described in detail by Bulusheva et al.[40] The intensity of G' band has been previously found to decrease with increase in total nitrogen level and is highly sensitive to pyridinic nitrogen type. Thus, compared to NGT(Co), NGT(Ni) and NGT(CoNi) contain higher content of pyridinic N, which is in good agreement with the XPS analysis.

The structure of carbon supports was also determined by Brunauer–Emmett–Teller (BET), using N_2 physisorption (at 77.35 K). **Figure 2e** and **Figure S1** show the nitrogen adsorption-desorption isotherms and pore size distribution curves of NGTs and Vulcan XC-72. The BET surface areas of NGT(Co), NGT(Ni), and NGT(CoNi) are 88.5, 77.8, and 123.1 m^2/g, respectively. Therefore, the NGT(CoNi) yielded much larger pore volume than NGT(Co) or NGT(Ni). Comparing to the surface areas of Vulcan XC-72 (208.5 m^2/g), those of NGTs are lower since the number of micropores in NGTs is much lower than that in Vulcan XC-72, which could be confirmed by pore size distribution (**Figure S1**). However, **Figure S1** presents that the NGTs have much more mesopores and macropores. Micropores may result in water flooding and may not be accessible in the electrolyte, meso- and macropores are favorable to mass transport during the electrochemical catalysis, thus NGTs can be more effective support in spite of lower surface areas. Pore size distribution and BET surface areas of different carbon supports are comprehensively compared and summarized in the **Figure S2** and **Table S1** in the supporting information.
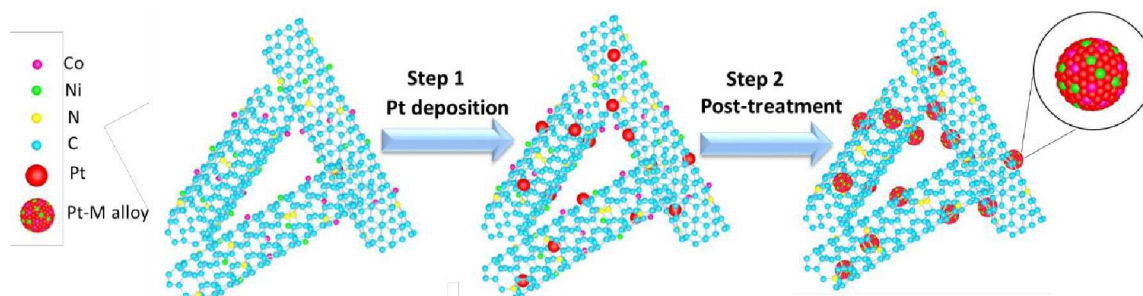
**Figure 1.** Scheme of the preparation process of post-Pt/NGT catalysts.

The presence of N in the prepared NGTs was confirmed by XPS (**Figure 2f**). The N 1s XPS spectra of graphene tubes showed two major nitrogen peaks at 401.1 eV and 398.9 eV, which can be assigned to graphitic and pyridinic nitrogen, respectively. It is believed that by doping pyridinic nitrogen sites in carbon matrix, more edge planes would be exposed and the carbon-derived catalysts can improve the ORR activity by facilitating the adsorption of reactive intermediates.[41,42] Moreover, the electronic structure of carbon can be altered by graphitic nitrogen in carbon planes, inducing catalytic ORR activity.[43] Notably, the content of graphitic N for NGT(Co) and NGT(CoNi) is higher than that for NGT(Ni), which is consistent with Raman results, where NGT(Co) and NGT(CoNi) showed higher graphitization degree. The XPS analysis for nitrogen-doped graphene tubes are comprehensively provided in **Figure S3** and their elemental quantification is summarized in **Table S2**.

To identify the crystal structure of NGT supports, X-ray diffraction (XRD) was performed (**Figure S4**). In addition to typical graphite carbon, the diffraction peaks around 2θ=44°, 52°, 76° indicate the presence of metals and oxides of Co or Ni species, indicating that some CoNi metals/oxides are still embedded or enclosed in the carbon matrix even after acid-leaching treatment. These retained metals and oxides of Co or Ni are further evidenced by XPS analysis (**Figure S3 and Figure S11**), which could be potentially beneficial for activity and stability enhancement.
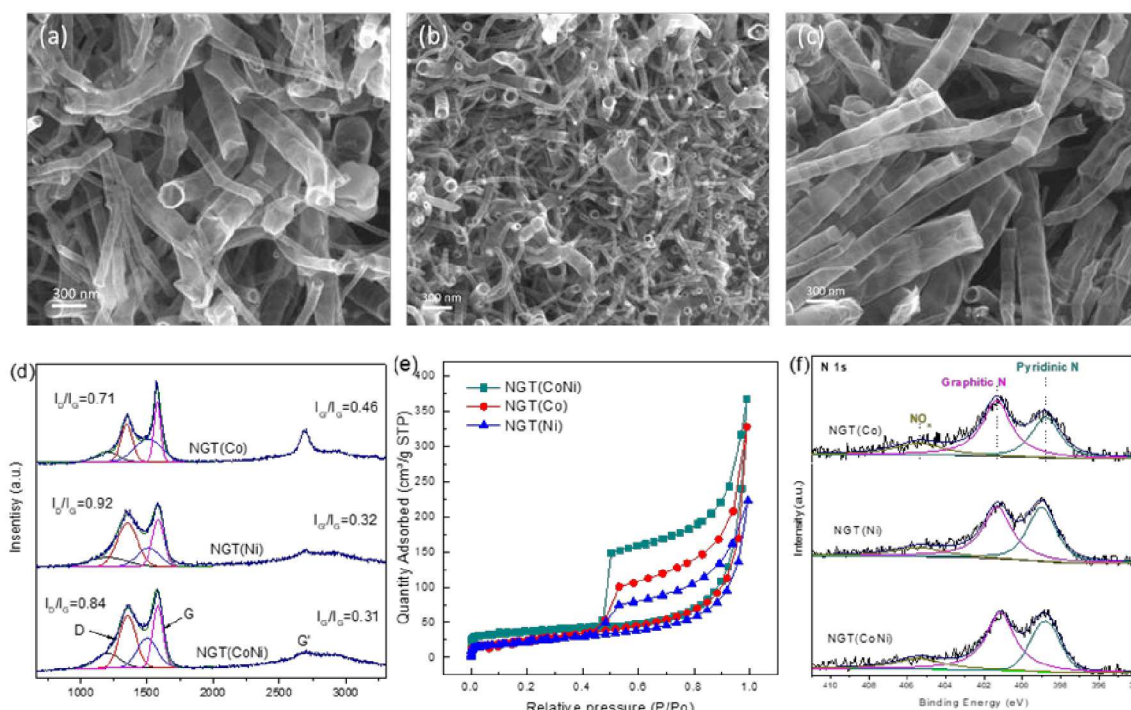
Figure 2. SEM images of (a) NGT(Co), (b) NGT(Ni), and (c) NGT(CoNi). Raman spectra (d), N_2 adsorption/desorption plots (e), and N 1s XPS spectra (f) of different graphene tube supports.

Nanoscale

ARTICLE
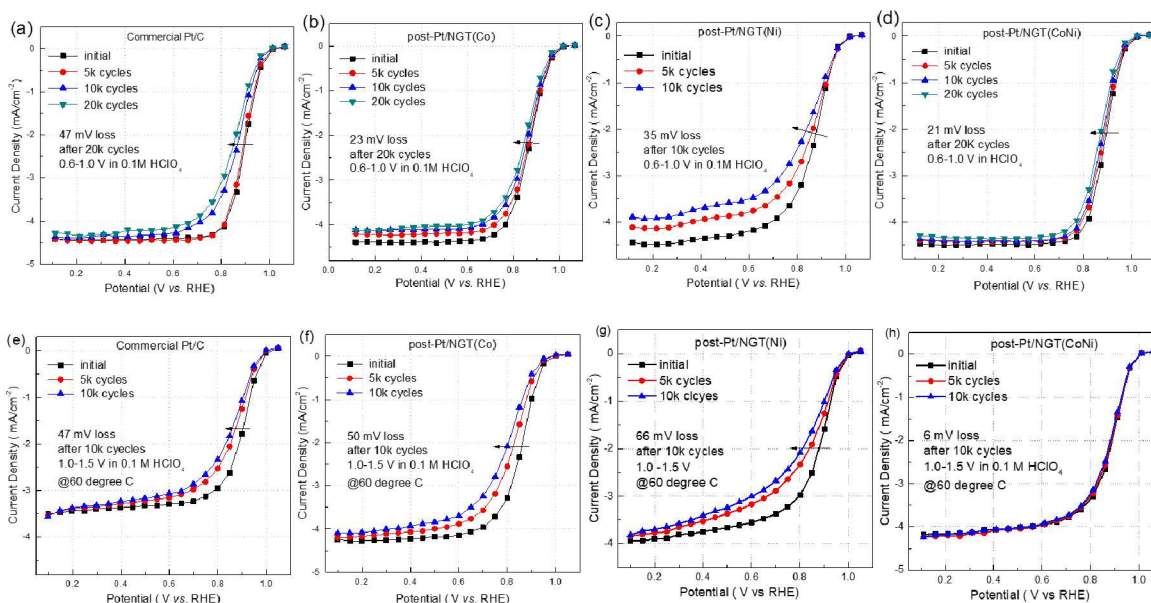
Figure 3. ORR steady-state polarization plots for (a, e) commercial Pt/C, (b, f) post-Pt/NGT(Co) catalyst, (c, g) post-Pt/NGT(Ni), and (d, h) post-Pt/NGT(CoNi) catalyst during ASTs. Potential cycling range from 0.6 to 1.0 V at a scan rate of 100 mV/s in 0.1 M HClO$_4$ at room temperature or range from 1.0 to 1.5 V at a scan rate of 500 mV/s in 0.1 M HClO$_4$ at 60 °C.

Stability screening of Pt on NGT supports

Electrochemical measurement of the Pt catalysts supported on various supports was performed using the rotating disk electrode (RDE) method. These Pt-based cathode catalysts were screened and compared to commercial Pt/C by accelerated stressed tests (ASTs) with different potential ranges which correspond to different degradation mechanism. Firstly, the stability of Pt-based nanoparticles was tested by performing cycles under the potential window from 0.6 to 1.0 V (vs. RHE) at room temperature in N$_2$-saturated 0.1 M HClO$_4$. As is shown in **Figure 3**, the half-wave potential and limit current density of post-Pt/NGT(Ni) decreased significantly, indicating that NGT(Ni) could not stabilize Pt nanoparticles during ASTs. This result is consistent with the result of N$_2$ isotherm and pore size distribution, which indicates the NGT(Ni) has the lowest BET surface area and poor pore distribution (**Figure 2e** and **Figure S1b**). Moreover, according to the SEM images, the Ni-derived graphene tubes showed the smallest diameter (50-100 nm), which possibly makes NGT(Ni) more difficult to obtain uniform metal particle dispersion. However, the Pt nanoparticles on NGT(Co) and NGT(CoNi) can be stabilized much better. Only

around 20 mV loss of E$_{1/2}$ was observed for post-Pt/NGT(Co) and post-Pt/NGT(CoNi) after 20,000 cycles. This suggests that both NGT(CoNi) and NGT(Co) can provide a better support effect than NGT(Ni) due to their relatively higher surface area and larger tube size along with other chemistry factors, which is discussed later. As for the commercial Pt/C catalyst, significant performance degradation (*ca*. 47 mV loss) was observed. The cyclic voltammetry plots were also recorded in **Figure S5**.

Next, we compared the stability of supports against oxidation by applying high potentials ranging from 1.0 to 1.5 V with a scan rate of 500 mV/s at room temperature. The cyclic voltammetry was plotted in **Figure S6**. ORR steady-state polarization plots were recorded in **Figure S7**. It can be seen that there was 10 mV loss of half-wave potential for commercial Pt/C and post-Pt/NGT(Ni) catalyst. However, interestingly, the activity of post-Pt/NGT(Co) and post-Pt/NGT(CoNi) catalysts is even improved in terms of half-wave potential during ASTs. Considering that the room temperature was not harsh enough to screen the stability of the studied carbon supports, electrochemical tests were further conducted at a temperature of 60 °C. As shown in **Figure 3**, after 10k cycles from 1.0-1.5 V at 60°C, the post-Pt/NGT(CoNi) performs the most promising result, only showing

6 mV loss in terms of $E_{1/2}$. Oppositely, commercial Pt/C, post-Pt/NGT(Co), and post-Pt/NGT(Ni) were degraded dramatically with losses of 47, 50, and 66 mV, respectively. This result indicated that NGT(CoNi) is the most stable carbon support under extremely severe conditions in terms of corrosion resistance due to its highly graphitized carbon structure. Therefore, the post-Pt/NGT(CoNi) catalyst not only exhibited better support effect to stabilize Pt nanoparticles but also displayed excellent carbon oxidation resistance. Therefore, we selected highly stable post-Pt/NGT(CoNi) catalyst to explore extensive structure and morphology characterization so as to identify the possible reasons to control the catalytic performance of Pt supported on graphene tube supports.

Improved performance and synergistic effect between Pt and nitrogen-doped graphene tube supports

To identify the potential reasons to control catalytic performance of these Pt supported on graphene tube catalysts, extensive electrochemical and physical characterization was performed. To reveal the crystal structure of Pt nanoparticles, X-ray diffraction (XRD) was performed on Pt cathode catalysts. As can be seen from **Figure 4b**, for the sample of Pt/NGT(CoNi), the four diffraction peaks at 2θ=39.8°, 46.3°, 67.7°, and 81.3° were consistent with those of pure Pt metal with an fcc structure, corresponding to the (111), (200), (220), and (311) planes, respectively. This result indicated that the Pt nanoparticles were successfully deposited on the carbon tubes. It should be noted that the peak position for Pt (200) crystal plane at 2θ=46.3° did not shift to higher angles, indicating that no alloy phase was formed. Importantly, after the post-treatment at 800 °C, the Pt crystal planes had a positive shift to higher angles, indicating that the Pt-M alloy structure was in-situ formed because of diffusion of transition metal from carbon into Pt fcc structure during the annealing process.[44] XRD results about alloy phase formation were consistent with XPS results (**Figure S8**) in that the Pt peak shifted to lower binding energy after post-treatment. The similar conclusion was also found for the catalyst of post-Pt/NGT(Co) and post-Pt/NGT(Ni) in **Figure S9**, which proved that pure Co or pure Ni can diffuse into the crystal lattice of Pt after the post-treatment at 800 °C, generating alloy structure. Notably, there was no obvious shift for the crystal peaks of Co or Ni, suggesting that the diffusion was unidirectional. Only Co or Ni embedded in the carbon tubes diffused to the surface and formed Pt-M (M is Co and Ni) alloy phase. This conclusion can also be confirmed by the fact that the relative intensities of the Pt peak and the CoNi peak have changed, which Pt-related peaks become more dominant.

The possible synergistic effect between Pt and graphene tubes can be confirmed by XPS and Raman data. The Pt 4f XPS spectra of Pt/NGT(CoNi) and post-Pt/NGT(CoNi) catalysts was displayed in **Figure S8**. The dominant peaks at ca. 71.4 eV and 74.7 eV can be assigned to metallic Pt, suggesting that most Pt ions have been fully reduced and deposited onto nitrogen-doped graphene tubes. Compared with Pt without carbon support (the doublet peaks are near 70.8 and 74.2 eV), the positive shift of Pt peaks could be possibly attributed to the strong interaction between Pt and support, which can benefit for the Pt stabilization.[30, 45] On the other hand, according to N

1s XPS spectra of NGT(CoNi) in **Figure 4c**, the graphitic and pyridinic nitrogen corresponding to peaks at 401.1 eV and 398.9 eV were dominant. Due to the strong electron donor behavior of nitrogen and the enhanced π-bonding, the introduction of nitrogen into the graphitic carbon matrix has been believed to be a useful strategy to attach Pt nanoparticles and produce stable Pt catalyst.[46, 47] Interestingly, the peak position of the N 1s spectrum was clearly shifted to higher binding energy after Pt deposition, indicating that the local electron density was changed by the possible interaction between N and Pt. It has been reported that such interaction could facilitate the Pt deposition and enhance the catalytic performance by inhibiting the agglomeration of nanoparticles and modifying the electronic structure of the catalysts.[30, 48] **Figure S10** showed several C 1s peaks of NGT(CoNi) supports and Pt-based catalysts which are related to miscellaneous carbon moieties and π–π* interaction between different graphene layers.[49] The Co 2p and Ni 2p peaks were exhibited in the **Figure S11**, which proved the presence of metallic Co and Ni. Raman characterization was shown in **Figure 4d**. The degree of graphitization was initially similar in NGT(CoNi) and Pt/NGT(CoNi). However, the graphitization degree of Pt/NGT(CoNi) became higher after post-treatment, which can possibly be attributed to the change of carbon structure modified by Pt nanoparticles during annealing process. It should be noted that the change in graphitization degree of NGT(CoNi) and post-NGT(CoNi) is negligible, proving that the presence of Pt is necessary to increase the degree of graphitization during post-treatment (**Figure S12**). Thus, not only can the nitrogen-doped graphene tubes provide strong interaction with Pt, but also the Pt can further increase the graphitization degree of graphene tubes. This synergistic interaction between Pt and carbon supports benefits excellent stability of Pt/NGT(CoNi) cathode catalysts.
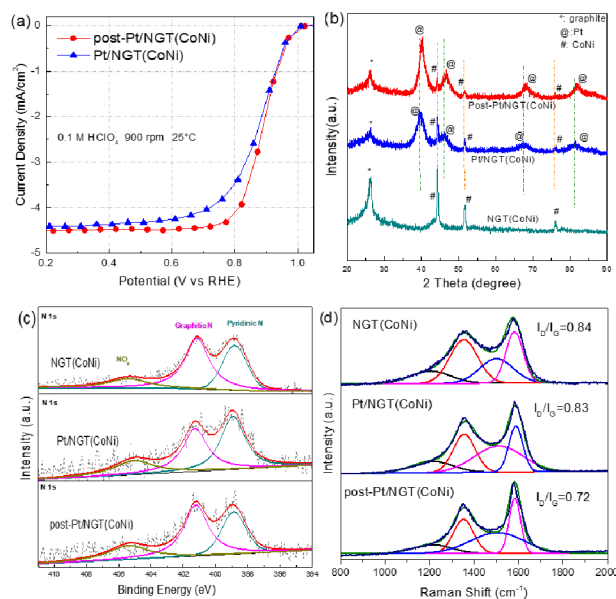

Figure 4. (a) Steady-state polarization plots for Pt/NGT(CoNi) and post-Pt/NGT(CoNi) in O_2-saturated 0.1 M $HClO_4$ at room temperature with rotation rate of 900 rpm. (b) XRD patterns for

NGT(CoNi) supports, Pt/NGT(CoNi), and post-Pt/NGT(CoNi). (c) N 1s XPS spectra of NGT(CoNi), Pt/NGT(CoNi), and post-Pt/NGT(CoNi). (d) Raman spectra of NGT(CoNi), Pt/NGT(CoNi) and post-Pt/NGT(CoNi).

Obviously, as shown in **Figure 4a**, the onset potential and half-wave potential of post-Pt/NGT(CoNi) were positively shifted slightly relative to Pt/NGT(CoNi), indicating that the activity was further improved due to the formation of Pt-M alloy structure in the post-treatment process.[3, 17, 50, 51] Moreover, NGT(CoNi) provided additional ORR active sites of nitrogen/metal co-doped carbon support, which can be evidenced by comparison between NGT(CoNi) and Vulcan XC-72 in RDE performance (**Figure S13**). Comparison of mass activities and specific

activities for commercial Pt/C, Pt/NGT(CoNi), and post-Pt/NGT(CoNi) at 0.85 V and 0.9 V was summarized in **Figure S14**, where the post-Pt/NGT(CoNi) showed the best performance than the others. This improved ORR activity of the post-Pt/NGT(CoNi) catalyst compared to traditional pristine XC-72 supports can be likely attributed to four possible reasons: (i) nitrogen and transition metal co-doped graphene tubes are inherently active for the ORR; (ii) the synergetic interaction between supports and Pt modifies electronic structure of Pt to enhance the ORR activity; (iii) the formation of Pt-M alloy further increases the ORR kinetics; (iv) the mass transfer is more favorable due to more mesopores and macropores on the NGT support. Also, the stability of catalysts was improved by post-treatment. The post-Pt/NGT(CoNi) showed much less ECSA loss rate than Pt/NGT(CoNi) (**Figure S15**).
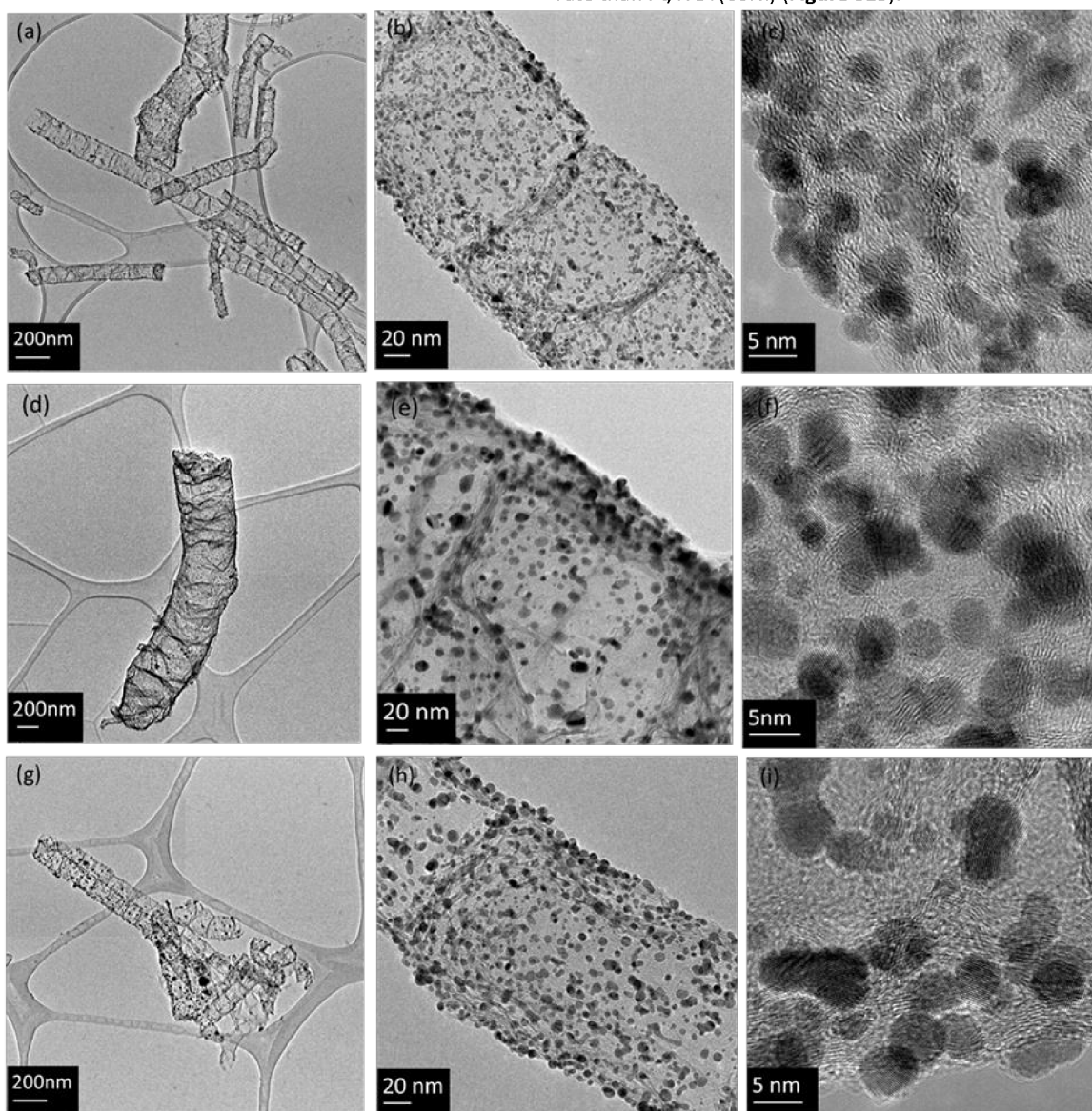
Figure 5. TEM and HR-TEM images of (a, b, and c) fresh post-Pt/NGT(CoNi), (d, e, and f) post-Pt/NGT(CoNi) after 20k cycles from 0.6-1.0 V vs. RHE, and (g, h, and i) post-Pt/NGT(CoNi) after 30k cycles from 1.0-1.5 V vs RHE.

Nanoscale

ARTICLE

To get more understanding of degradation mechanisms for catalysts during ASTs with different potential ranges, the TEM characterization was performed on fresh post-Pt/NGT(CoNi), post-Pt/NGT(CoNi) after 20k cycles from 0.6-1.0 V vs. RHE, and post-Pt/NGT(CoNi) after 30k cycles from 1.0-1.5 V vs. RHE, which was shown in **Figure 5**. The tube structure was apparently well defined and the Pt nanoparticles were uniformly deposited on nitrogen-doped carbon tubes with a narrow distribution (**Figure S16d**). As was shown in HR-TEM image (**Figure 5c**), the deposited Pt nanoparticles were highly crystallized. Notably, the particle size distribution of Pt on fresh catalyst, measured from 100 nanoparticles, indicated that the average particle diameter was around 3.7 nm, which was larger than that on commercial Pt/C (2.7 nm). These results are consistent with the XRD data, where the crystallinity of Pt on NGTs was higher (**Figure 17)**. As mentioned above, commercial Pt/C catalyst showed a 47 mV loss of $E_{1/2}$ after 20k cycles (0.6-1.0 V), while the post-Pt/NGT(CoNi) catalyst exhibited only 21 mV loss of $E_{1/2}$, suggesting that the Pt metal on NGT(CoNi) is much more stable than that on Vulcan XC-72. To further identify the loss in activity, **Figure S18a** shows the normalized ECSA calculated for commercial Pt/C and post-Pt/NGT(CoNi) catalysts as a function of cycle. The ECSA of commercial Pt/C catalysts decreases dramatically as the number of cycles increases and only 33% of initial ECSA value of Pt/C catalyst was retained after 20,000 cycles. Surprisingly, more than 67% of initial ECSA of post-Pt/NGT(CoNi) catalyst was maintained, indicating the higher stability of Pt nanoparticles on NGTs than that on Vulcan XC-72. As shown in **Figure 5d-f** and **Figure S16e**, the mean particle size of the Pt on NGT(CoNi) became 5.3 nm after 20,000 cycles from 0.6-1.0 V, indicating that this catalyst still exhibited good Pt dispersion and no extensive agglomeration was observed. Notably, the Pt-M (M is Co and Ni) alloy structure was in-situ formed during the post-treatment. The stability difference of Pt metals between post-Pt/NGT(CoNi) and commercial Pt/C catalyst is possibly attributed to the difference in Pt oxidation potential and dissolution potential. It has been reported that the Pt oxides formation potential on Pt-based alloy catalysts would be shifted to higher values when compared to pure Pt.[52, 53] Moreover, the Pt dissolution potential would also be changed while the Pt nanoparticle sizes are modified.[54, 55] Additionally, the stronger binding derived from the synergistic effect between Pt and nitrogen-doped carbon support can lead to higher stability of Pt nanoparticles.[29, 30, 56]

As for the stability of carbon supports against oxidation, **Figure S18b** presents that the commercial Pt/C catalyst showed a steady decrease in ECSA values during ASTs within 1.0-1.5 V at room temperature, which can be attributed to Pt nanoparticle detachment or agglomeration on the carbon supports. The amorphous carbon structure especially micropores on Vulcan XC-72 would be collapsed or destroyed.[56] And this ECSA loss was also related to Pt agglomeration on the oxidized carbon support.[58] After 20,000 cycles, only 65% of initial ECSA of Pt/C catalysts was maintained. Surprisingly, the ECSA of post-Pt/NGT(CoNi) catalyst were increased after 30,000 potential cycles (**Figure S18b**) and the average size of Pt nanoparticle increased to 4.6 nm (**Figure 5g-i and Figure S16f**). Because the transition metal or metal oxides embedded in the carbon matrix can be dissolved into the electrolyte by applying potential and the active surface area became higher which was favorable for exposure of active sites. This result is consistent with the results of HR-TEM (**Figure 5g**), in which the tube structure was well maintained after 30,000 cycles from 1.0-1.5 V in 0.1 M HClO$_4$, indicating that the novel NGT(CoNi) is corrosion-resistant, so that the Pt detachment and agglomeration was alleviated. As for the tests at an elevated temperature of 60 °C, it was clear that the commercial Pt/C catalyst has undergone tremendous degradation in performance. On the contrary, our post-Pt/NGT(CoNi) catalyst still maintained excellent activity under high-temperature conditions and the performance degradation was negligible. This result was further evidenced by TEM characterization (**Figure S19**) where the tube structure was well maintained so that Pt nanoparticles still maintained good dispersion with a narrow distribution. The more durable behavior of post-Pt/NGT(CoNi) at high potential window was considered to stem from the durable graphene tubes support, which had intrinsic higher degree of graphitization than Vulcan XC-72 (**Figure S20**) and was further increased by post-treatment (**Figure 4d**) so that detachment and agglomeration of Pt particles were greatly alleviated.

Conclusions

In summary, a highly active and stable Pt alloy cathode catalyst was developed based on a support of novel nitrogen/metal co-doped graphene tubes. Among three carbon tubes derived from various transition metals we studied, the NGT(CoNi) is the most promising support due to its highly graphitized carbon structure and large tube size, which benefit for the corrosion resistance and Pt dispersion. The improved ORR activity of post-Pt/NGT(CoNi) catalysts is possibly attributed to the formation of Pt-M alloy phase, intrinsic active sites supplied by nitrogen/metal co-doped graphene tubes, synergistic effect between Pt and nitrogen-doped carbon support, and enhanced mass transfer due to appropriate mesopore/macropore distribution. More importantly, the novel post-Pt/NGT(CoNi)

catalyst shows excellent stability at both low and high potential ranges, which is ascribed to the highly graphitized carbon matrix, providing excellent support effect, mitigating the agglomeration of Pt nanoparticles and carbon corrosion. Therefore, this research demonstrates a new Pt alloy catalyst and novel carbon support for the cathode of fuel cells with both excellent catalytic activity and stability.

Conflicts of interest

There are no conflicts to declare.

Acknowledgment

References

1   G. Wu, K. L. More, C. M. Johnston and P. Zelenay, *Science*, **2011**, 332, 443-447.
2   R. Borup, J. Meyers, B. Pivovar, Y. S. Kim, R. Mukundan, N. Garland, D. Myers, M. Wilson, F. Garzon and D. Wood, *Chem. Rev.*, 2007, **107**, 3904-3951.
3   Y. Bing, H. Liu, L. Zhang, D. Ghosh and J. Zhang, *Chem. Soc. Rev.*, 2010, **39**, 2184-2202.
4   Y. Nie, L. Li and Z. Wei, *Chem. Soc. Rev.*, 2015, **44**, 2168-2201.
5   X. Li, H. R. Colón-Mercado, G. Wu, J.-W. Lee and B. N. Popov, *Electrochem. Solid-State Lett.*, 2007, **10**, B201-B205.
6   S. Mitsushima, S. Kawahara, K.-i. Ota and N. Kamiya, *J. Electro. Soc.*, 2007, **154**, B153-B158.
7   S.-Y. Huang, P. Ganesan, S. Park and B. N. Popov, *J. Am. Chem. Soc.*, 2009, **131**, 13898-13899.
8   M. K. Debe, *Nature*, 2012, **486**, 43-51.
9   L. Ding, A. Wang, G. Li, Z. Liu, Z. Whao, C. Su and Y. Tong, *J. Am. Chem. Soc.* 2012, **134**, 5730.
10 X. X. Wang, S. Hwang, Y.-T. Pan, K. Chen, Y. He, S. Karakalos, H. Zhang, J. S. Spendelow, D. Su and G. Wu, *Nano Lett.*, 2018, 18, 4163-4171.
11 V. R. Stamenkovic, B. Fowler, B. S. Mun, G. Wang, P. N. Ross, C. A. Lucas and N. M. Marković, *Science*, 2007, **315**, 493-497.
12 C. Cui, L. Gan, L.-H. Li, S.-H. Yu, M. Heggen and P. Strasser, *Nano Lett.*, 2012, **12**, 5885-5889.
13 M.-k. Min, J. Cho, K. Cho and H. Kim, *Electrochim. Acta*, 2000, **45**, 4211-4217.
14 A. Arico, A. Shukla, H. Kim, S. Park, M. Min and V. Antonucci, *Appl. Surf. Sci.*, 2001, **172**, 33-40.
15 P. Mani, R. Srivastava and P. Strasser, *J. Power Sources*, 2011, **196**, 666-673.
16 Q. Jia, K. Caldwell, K. Strickland, J. M. Ziegelbauer, Z. Liu, Z. Yu, D. E. Ramaker and S. Mukerjee, *ACS Catal.*, 2014, **5**, 176-186.
17 C. Chen, Y. Kang, Z. Huo, Z. Zhu, W. Huang, H. L. Xin, J. D. Snyder, D. Li, J. A. Herron and M. Mavrikakis, *Science*, 2014, **343**, 1339-1343.
18 T. Toda, H. Igarashi, H. Uchida and M. Watanabe, *J. Electrochem. Soc.*, 1999, **146**, 3750-3756.
19 G. Wu, Y.-S. Chen and B.-Q. Xu, *Electrochem. Comm.*, 2005, **7**, 1237-1243.
20 Z. Liu, L. M. Gan, L. Hong, W. Chen and J. Y. Lee, *J. Power Sources*, 2005, **139**, 73-78.
21 Y. Mu, H. Liang, J. Hu, L. Jiang and L. Wan, *The J. Phys. Chem. B*, 2005, **109**, 22212-22216.
22 C. Zhu and S. Dong, *Nanoscale*, 2013, **5**, 1753-1767.
23 D. Higgins, M. A. Hoque, M. H. Seo, R. Wang, F. Hassan, J. Y. Choi, M. Pritzker, A. Yu, J. Zhang and Z. Chen, *Adv. Func. Mater.*, 2014, **24**, 4324-4324.
24 S. Kundu, T. C. Nagaiah, X. Chen, W. Xia, M. Bron, W. Schuhmann and M. Muhler, *Carbon*, 2012, **50**, 4534-4542.
25 G. Wu, A. Santandreu, W. Kellogg, S. Gupta, O. Ogoke, H. Zhang, H.-L. Wang and L. Dai, *Nano Energy*, 2016, **29**, 83-110.
26 X. X. Wang, D. A. Cullen, Y.-T. Pan, S. Hwang, M. Wang, Z. Feng, J. Wang, M. H. Engelhard, H. Zhang, Y. He, Y. Shao, D. Su, K. L. More, J. S. Spendelow and G. Wu, *Advanced Materials*, 2018, **30**, 1706758.
27 M. Chen, L. Wang, H. Yang, S. Zhao, H. Xu and G. Wu, *J. Power Sources*, 2018, **375**, 277-290.
28 H. Zhang, S. Hwang, M. Wang, Z. Feng, S. Karakalos, L. Luo, Z. Qiao, X. Xie, C. Wang, D. Su, Y. Shao and G. Wu, *J. Am. Chem. Soc.*, 2017, **139**, 14143-14149.
29 X. Wang, Q. Li, H. Pan, Y. Lin, Y. Ke, H. Sheng, M. T. Swihart and G. Wu, *Nanoscale*, 2015, **7**, 20290-20298.
30 Y. Chen, J. Wang, H. Liu, R. Li, X. Sun, S. Ye and S. Knights, *Electrochem. Comm.*, 2009, **11**, 2071-2076.
31 R. I. Jafri, N. Rajalakshmi and S. Ramaprabhu, *J. Mater. Chem.*, 2010, **20**, 7114-7117.
32 Q. Li, H. Pan, D. Higgins, R. Cao, G. Zhang, H. Lv, K. Wu, J. Cho and G. Wu, *Small*, 2015, **11**, 1443-1452.
33 C. C. Winterbourn, Toxicology Letters. 1995, **82-83**, 969-974.
34 T. Porwol, W. Ehleben, K. Zie, J. Fandrey, H. Acker, *Eur. J. Biochem.*,1998, **256**, 16223.
35 A.Cuesta, P.Dhamelincourt, J.Laureyns, A.Martínez-Alonso, J.M.D.Tascón, *Carbon* 1994, **32** (8), 1523-1532.
36 F. Bonhomme, J. C. Lassègues and L. Servant, *J. Electrochem. Soc.*, 2001, **148**, E450-E458.
37 L.M.Malard, M.A.Pimenta, G.Dresselhaus, M.S.Dresselhaus, *Phys. Rep.*, 2009, **473**, 51-87
38 A. C.Ferrari, *Solid State Commun.*, 2007, **143**, 47–57
39 A. Reina, X. Jia, J. Ho, D. Nezich, H. Son, V. Bulovic, M. S. Dresselhaus and J. Kong, *Nano Lett.*, 2009, **1**, 30-35.
40 L. G. Bulusheva, A. V. Okotrub, I. A. Kinloch, I. P. Asanov, A. G. Kurenya, A. G. Kudashov, X. Chen and H. Song., *Physica Status solidi (b)* 2008, **245**, 1971-1974
41 S. Maldonado and K. J. Stevenson, *J. Phys. Chem. B*, 2005, **109**, 4707-4716.
42 P. H. Matter, L. Zhang and U. S. Ozkan, *J. Catal.*, 2006, **239**, 83-96.
43 G. Wu, K. L. More, P. Xu, H.-L. Wang, M. Ferrandon, A. J. Kropf, D. J. Myers, S. Ma, C. M. Johnston and P. Zelenay, *Chem. Comm.*, 2013, **49**, 3291-3293.
44 W. Jung, T. Xie, T. Kim, P. Ganesan and B. N. Popov, *Electrochim. Acta*, 2015, **167**, 1-12.
45 W. An and C. H. Turner, *J. Phys. Chem. C*, 2009, **113**, 7069-7078.
46 Y. Shao, G. Yin and Y. Gao, *J. Power Sources*, 2007, **171**, 558-566.
47 M. S. Saha, R. Li, X. Sun and S. Ye, *Electrochem. Comm.*, 2009, **11**, 438-441.
48 G. Wu, D. Li, C. Dai, D. Wang and N. Li, *Langmuir*, 2008, **24**, 3566-3575.
49 S. Gupta, L. Qiao, S. Zhao, H. Xu, Y. Lin, S. V. Devaguptapu, X. Wang, M. T. Swihart and G. Wu, *Adv. Energy Mater.*, 2016, **6**, 1601198.

50 H. A. Gasteiger, S. S. Kocha, B. Sompalli and F. T. Wagner, *Appl. Catal., B*, 2005, **56**, 9-35.

51 C. Cui, L. Gan, M. Heggen, S. Rudi and P. Strasser, *Nature Mater.*, 2013, **12**, 765.

52 T. Xie, W. Jung, T. Kim, P. Ganesan and B. N. Popov, *J. Electrochem. Soc.*, 2014, **161**, F1489-F1501.

53 U. Paulus, A. Wokaun, G. Scherer, T. Schmidt, V. Stamenkovic, V. Radmilovic, N. Markovic and P. Ross, *J. Phys. Chem. B*, 2002, **106**, 4181-4191.

54 L. Tang, B. Han, K. Persson, C. Friesen, T. He, K. Sieradzki and G. Ceder, *J. Am. Chem. Soc.*, 2009, **132**, 596-600.

55 E. F. Holby, W. Sheng, Y. Shao-Horn and D. Morgan, *Energy Environ. Sci.*, 2009, **2**, 865-871.

56 Y. Zhou, K. Neyerlin, T. S. Olson, S. Pylypenko, J. Bult, H. N. Dinh, T. Gennett, Z. Shao and R. O'Hayre, *Energy Environ. Sci.*, 2010, **3**, 1437-1446.

57 F. Hasché, M. Oezaslan and P. Strasser, *Phys. Chem. Chem. Phys.*, 2010, **12**, 15251-15258.

58 Z. Chen, M. Waje, W. Li and Y. Yan, *Angew. Chem. Int. Ed.*, 2007, **46**, 4060-4063.